



Wave breaking in the surf zone and deep-water in a non-hydrostatic RANS model. Part 1: Organized wave motions

Morteza Derakhti^{a,*}, James T. Kirby^a, Fengyan Shi^a, Gangfeng Ma^b

^aCenter for Applied Coastal Research, University of Delaware, Newark, DE, USA

^bDepartment of Civil and Environmental Engineering, Old Dominion University, Norfolk, VA, USA

ARTICLE INFO

Article history:

Received 26 June 2015

Revised 10 August 2016

Accepted 8 September 2016

Available online 20 September 2016

Keywords:

Non-hydrostatic wave models

Breaking waves

Wave energy dissipation

ABSTRACT

We examine wave-breaking predictions ranging from shallow- to deep-water conditions using a non-hydrostatic σ -coordinate RANS model NHWAVE as described in Derakhti et al. (2016a), comparing results both with corresponding experiments and with the results of a volume-of-fluid (VOF)/Navier-Stokes solver (Ma et al., 2011; Derakhti and Kirby, 2014a,b). Our study includes regular and irregular depth-limited breaking waves on planar and barred beaches as well as steepness-limited unsteady breaking focused wave packets in intermediate and deep water. In Part 1 of this paper, it is shown that the model resolves organized wave motions in terms of free-surface evolution, spectral evolution, organized wave velocity evolution and wave statistics, using a few vertical σ -levels. In addition, the relative contribution of modeled physical dissipation and numerical dissipation to the integral breaking-induced wave energy loss is discussed. In steepness-limited unsteady breaking focused wave packets, the turbulence model has not been triggered, and all the dissipation is imposed indirectly by the numerical scheme. Although the total wave-breaking-induced energy dissipation is underestimated in the unsteady wave packets, the model is capable of predicting the dispersive and nonlinear properties of different wave packet components before and after the break point, as well as the overall wave height decay and the evolution of organized wave velocity field and power spectrum density over the breaking region. In Part 2 (Derakhti et al., 2016b), model reproduction of wave-breaking-induced turbulence and mean circulation is examined in detail. The same equations and numerical methods are used for the various depth regimes, and no ad-hoc treatment, such as imposing hydrostatic conditions, is involved in triggering breaking. Vertical grid resolution in all simulated cases is at least an order of magnitude coarser than that of typical VOF-based simulations.

© 2016 Elsevier Ltd. All rights reserved.

1. Introduction

One of the least understood and yet most important events in the ocean upper layer is the breaking of surface waves. Surface wave breaking, a complex, two-phase flow phenomenon, plays an important role in numerous environmental and technical processes such as air-sea interaction, acoustic underwater communications, optical properties of the water column, nearshore mixing and coastal morphodynamics (Peregrine, 1983; Battjes, 1988; Banner and Peregrine, 1993; Melville, 1996; Brocchini and Peregrine, 2001a; 2001b; Perlin et al., 2013).

Although high-resolution frameworks such as large-eddy simulations (LES) combined with the volume-of-fluid (VOF) method

for free-surface tracking (Watanabe et al., 2005; Lakehal and Liovic, 2011; Derakhti and Kirby, 2014a; Zhou et al., 2014; Lubin and Glockner, 2015) can resolve small scale processes such as wave-breaking-induced turbulent coherent structures, they are still computationally expensive even for laboratory-scale events. A lower-resolution three-dimensional (3-D) framework is needed to study long-term, $O(\text{days})$, and large-scale, $O(100 \text{ m} \approx 10 \text{ km})$, wave-breaking-driven circulation as well as transport of sediment, bubbles, and other suspended materials. Over the past decade, several 3-D wave-resolving non-hydrostatic models based on Reynolds-averaged Navier-Stokes (RANS) equations using a surface- and terrain-following grid have been developed for coastal applications (Lin and Li, 2002; Zijlema et al., 2011; Bradford, 2011; Ma et al., 2012; Shirkavand and Badiei, 2014).

The non-hydrostatic model NHWAVE is originally described in Ma et al. (2012). NHWAVE solves the RANS equations formulated in time-dependent, surface- and terrain-following curvilinear

* Corresponding author.

E-mail address: derakhti@udel.edu (M. Derakhti).

(x, y, σ) coordinates, hereafter referred as the σ -coordinate system. The governing equations are discretized by a combined finite-volume/finite-difference approach with a Godunov-type shock-capturing scheme. The model is wave-resolving and can provide instantaneous descriptions of surface displacement and wave orbital velocities. Note that for relatively short waves or in the case of the existence of a large vertical velocity gradient, an adequate number of vertical σ -levels is needed to resolve the corresponding velocity field. The model has been applied to study tsunami wave generation by submarine landslides (Ma et al., 2013a, 2015; Tappin et al., 2014), wave damping in vegetated environments (Ma et al., 2013b), nearshore suspended sediment transport (Ma et al., 2014a), wave interaction with porous structures (Ma et al., 2014b) and baroclinic mixing and breaking processes (Shi et al., 2015). In these studies as well as in most of the previous comparable non-hydrostatic studies using a terrain-following grid (e.g., Lin and Li, 2002; Bradford, 2011), the effects of surface and bottom slopes in the dynamic boundary conditions at the top and bottom interfaces, e.g., the continuity of the tangential surface stress, were ignored. Derakhti et al. (2016a) have recently derived a new form of the governing equations together with consistent surface and bottom boundary conditions. By examining the predicted velocity field in a deep-water standing wave in a closed basin, they found that the consistent boundary conditions did not generate unphysical vorticity at the free surface, in contrast to commonly used, simplified stress boundary conditions developed by ignoring all contributions except vertical shear in the transformation of stress terms. They also showed that surface slope effects should be taken into account in order to accurately resolve turbulence statistics, such as turbulent kinetic energy distribution, in surf zone breaking waves.

The relevant literature on non-hydrostatic model predictions of surface wave breaking using a surface- and terrain-following grid is mainly related to depth-limited breaking waves and mostly focuses on the capability of this framework to predict free surface evolution and wave statistics, while less attention has been dedicated to velocity and turbulence fields. Although there are recent studies (Young and Wu, 2010; Ai et al., 2014) examining the capability of non-hydrostatic models to resolve wave-wave nonlinear interaction and dispersion properties of non-breaking deep-water waves, no study has examined non-hydrostatic model predictions of wave-breaking-related processes in steepness-limited unsteady breaking waves.

During active breaking, perhaps the major simplification by any non-hydrostatic model using a surface- and terrain-following grid is achieved by replacing a complex free surface by a single-valued function of horizontal location. Instead of having a jet/splash cycle in plunging breakers or formation of surface rollers and a turbulent bore in spilling breakers, this simplification leads to the formation of a relatively sharp wave-front as a wave approaches breaking, and thus detailed near-surface processes during active breaking, such as turbulence generation and air entrainment, cannot be resolved. The tangential stress at the locally smooth free surface should include the Reynolds stress in the case of the existence of high turbulence near the free surface such as in the bore-front region (see, for more details, Brocchini and Peregrine, 2001b, Section 5). To the knowledge of the authors, all of the available non-hydrostatic models, including NHWAVE, assume zero tangential stress boundary condition at the locally smooth free surface, resulting in an underestimation of near-surface turbulent stresses and physical wave-breaking-induced energy dissipation during active breaking.

Using an appropriate shock-capturing numerical scheme, the sharp wave-front propagates without any unphysical numerical oscillation. Numerical dissipation is inherently imposed by a selected limiter in regions with large horizontal velocity gradient, analogous

to a hydraulic jump. This inherent numerical dissipation may compensate the lack of physical energy dissipation during active breaking; without defining any criterion and/or tunable model parameters to detect the location of breaking and the associated energy dissipation. For surf zone breaking waves, when non-hydrostatic effects are retained, Smit et al. (2013) emphasized that high resolution in the vertical direction (more than 15 levels) is needed for reasonable integral energy dissipation and corresponding wave-height decay resulting from the sharp wave-front propagation in the non-hydrostatic RANS model SWASH (Zijlema et al., 2011). In place of common shock-capturing schemes (Toro, 2009), they used a special treatment to maintain momentum conservation across flow discontinuities, observing that insufficient vertical resolution led to an underestimation of velocities, thereby delaying the initiation of breaking. Following Tonelli and Petti (2010), they proposed a hydrostatic front approximation in which the non-hydrostatic part of pressure is switched off by analogy to the nonlinear shallow water equations. Three model parameters were introduced to determine a region at which the non-hydrostatic part of pressure is switched off, and to suppress the artificial generation of high-frequency oscillations due to the discrete activation of the switching. Using this technique, SWASH was shown to predict the evolution of wave-height statistics in the surf zone reasonably well compared with laboratory measurements of irregular waves, by using two vertical levels.

Our goals here are (1) to carefully examine what level of detail of organized wave motions as well as wave-breaking-induced turbulence and mean circulation can be reproduced by the non-hydrostatic model NHWAVE as described by Derakhti et al. (2016a), across the inner shelf and nearshore regions, and (2) to establish whether this model is capable of providing accurate representations of breaking-wave properties in intermediate and deep water. Our study includes regular and irregular depth-limited breaking waves over planar and barred beaches as well as steepness-limited unsteady breaking focused wave packets. In Part 1 of this paper, NHWAVE predictions of organized wave motions in terms of free-surface evolution, spectral evolution, organized wave velocity evolution and wave statistics are investigated. In Part 2 (Derakhti et al., 2016b), the model capability and accuracy in the reproduction of wave-breaking-induced turbulence and mean circulation are examined in detail.

The paper is organized as follows. A brief description of the model is presented in Section 2. Details of the numerical set-up, and comparisons of model results with measurements for depth-limited breaking waves on planar and barred beaches are given in Section 3. Details of the numerical set-up, and comparisons of model results with measurements and with results of VOF/LES simulations of Derakhti and Kirby (2014a,b) for steepness-limited unsteady breaking focused wave packets are given in Section 4. The relative contribution of modeled physical energy dissipation and numerical dissipation is discussed in Section 5. Conclusions are presented in Section 6.

2. Mathematical formulation

Here, we present a brief summary of governing equations and dynamic surface boundary conditions. The reader is referred to Derakhti et al. (2016a) for details of the governing equations and boundary conditions. Details of the numerical method may be found in Ma et al. (2012) and Derakhti et al. (2015).

2.1. Governing equations

Assuming a uniform density and atmospheric pressure fields, the continuity and momentum equations in the σ -coordinate

$(t = t', x = x', y = y', \sigma = \frac{z' + h}{D})$ system are given by (Derakhti et al., 2016a)

$$\frac{\partial D}{\partial t} + \frac{\partial U_i}{\partial x_i} \lambda_i + \frac{\partial \Omega}{\partial \sigma} = 0 \quad (1)$$

$$\begin{aligned} \frac{\partial U_i}{\partial t} + \frac{\partial}{\partial x_j} \left\{ U_i U_j / D + [g\eta h + g\eta^2/2] \delta_{ij} \right\} \lambda_j + \frac{\partial U_i \Omega / D}{\partial \sigma} \\ = g\eta h_{x_i} \lambda_i - \frac{1}{\rho_0} \left\{ \frac{\partial \mathcal{P}}{\partial x_i} \lambda_i + \frac{\partial \sigma_{x'_i} \mathcal{P}}{\partial \sigma} \right\} + \frac{\partial 2(v_{eff})_j \mathcal{E}_{ij}}{\partial x_j} \lambda_j \\ + \frac{\partial 2\sigma_{x'_j} (v_{eff})_j \mathcal{E}_{ij}}{\partial \sigma}, \end{aligned} \quad (2)$$

where $(i, j) = 1, 2, 3$, and $\lambda_j = 1 - \delta_{3j}$ where hereafter summation inside expressions involving λ_j is not implied. g is the gravitational acceleration, ρ_0 is the reference water density, superscript $(')$ refers to Cartesian coordinates (t', x', y', z') , δ is the Kronecker delta function, $(\chi) = \partial(\chi)/\partial \chi$, and

$$\begin{aligned} U_i &= Du_i \\ \Omega &= D\sigma_t + \sigma_{x'_j} U_j \\ \mathcal{P} &= D \left\{ p^d + \frac{1}{3} \tau_{kk} \right\} \\ \mathcal{E}_{ij} &= \frac{1}{2} \left\{ \frac{\partial U_i}{\partial x_j} \lambda_j + \frac{\partial U_j}{\partial x_i} \lambda_i + \frac{\partial}{\partial \sigma} (\sigma_{x'_j} U_i + \sigma_{x'_i} U_j) \right\}, \end{aligned} \quad (3)$$

where u is the ensemble-averaged velocity, p^d is the ensemble-averaged dynamic pressure, τ is the stress term. Here, $D = h + \eta$ is the total water depth, h is the still water depth, and η is a locally smooth estimate of a spatial average of the free surface and can be considered as a single-valued mean air-water interface as defined in Brocchini and Peregrine (2001b, Figure 1). In Eq. (2), v_{eff} is the sum of the molecular and turbulent eddy viscosity. In this paper, the $k - \epsilon$ model based on the renormalization group theory (Yakhot et al., 1992) is used to estimate the latter (see Derakhti et al., 2016a, Section 2.3).

2.2. Surface and bottom boundary conditions

Assuming no mass flux at the interface, the kinematic surface and bottom boundary conditions in the σ -coordinate system are simply written as

$$W \Big|_{\sigma=0,1} = D\xi_t + \xi_x U \Big|_{\sigma=0,1} + \xi_y V \Big|_{\sigma=0,1} \quad (4)$$

where $\xi = \eta$ at the free surface ($\sigma = 1$), and $\xi = -h$ at the bottom ($\sigma = 0$).

Using the continuity of the tangential stress on the bottom and top boundaries ($\sigma = 0, 1$), Derakhti et al. (2016a, Section 3.2) showed that

$$\begin{aligned} \frac{\partial U_i}{\partial \sigma} \Big|_{\sigma=0,1} &= \frac{D^2}{A\rho_0 v_{eff}} \mathcal{F}_i^{ext} \Big|_{\sigma=0,1} - \xi_{x_i} \frac{\partial W}{\partial \sigma} \Big|_{\sigma=0,1} \\ &+ \frac{D}{A^2} \left\{ 2\xi_{x_i} (U_i)_{x_i} - [1 - \xi_{x_i}^2] (W)_{x_i} \right. \\ &\left. + \xi_{x_j} [(U_i)_{x_j} + (U_j)_{x_i} + \xi_{x_i} (W)_{x_j}] \right\}_{\sigma=0,1} \end{aligned} \quad (5)$$

where $(i, j) = (1, 2)$ or $(2, 1)$, $A = \sqrt{1 + \xi_x^2 + \xi_y^2}$, \mathcal{F}_i^{ext} is the external tangential stress, and

$$(U_i)_{x_j} = \partial U_i / \partial x_j - U_i D_{x_j} / D. \quad (6)$$

The external tangential stress at $\sigma = 1$ is a combination of the wind-induced shear stress and the Reynolds-type stress in the case of the existence of high turbulence near the free surface such as in the bore-front region (see, for more details, Brocchini and Peregrine, 2001b, Section 5). Parameterization of the latter is beyond

the scope of the present study; instead, we use $\mathcal{F}_i^{ext} \Big|_{\sigma=1} = 0$ in the entire numerical domain. The external shear stress near the bottom is approximated using the law of the wall, assuming a uniform bottom roughness height as in Derakhti et al. (2016a, Section 3.2).

Neglecting viscous stresses in the air side, the Dirichlet-type boundary condition for the modified ensemble-averaged dynamic pressure at $\sigma = 1$ reads as (Derakhti et al., 2016a, Section 3.3)

$$\begin{aligned} \mathcal{P} \Big|_{\sigma=1} &= -\frac{\rho_0 v_{eff} \Big|_{\sigma=1}}{A^2} \left\{ 2\xi_x [(W)_x - \xi_x (U)_x] \right. \\ &\left. + 2\xi_y [(W)_y - \xi_y (V)_y] - 2\xi_x \xi_y [(U)_y + (V)_x] \right\}_{\sigma=1}. \end{aligned} \quad (7)$$

At the bottom, however, such a relation cannot be applied unless the bottom is a dynamically coupled layer. By neglecting the Reynolds stress gradients at the bottom, a Neumann-type boundary condition for the modified dynamic pressure at the bottom reads as (Derakhti et al., 2016a, Section 3.3)

$$\frac{\partial \mathcal{P}}{\partial \sigma} \Big|_{\sigma=0} = -D\rho_0 \left\{ \frac{\partial W}{\partial t} + \frac{\partial WU/D}{\partial x} + \frac{\partial WV/D}{\partial y} \right\}_{\sigma=0}. \quad (8)$$

3. Depth-limited breaking waves

3.1. Model set-up and choice of experimental conditions

We consider model performance for the case of regular depth-limited wave breaking on a planar beach using the data set of Ting and Kirby (1994), and on a barred beach using the data set of Scott et al. (2004) in terms of the wave height as well as phase-averaged free-surface and orbital velocity evolution (Section 3.2). In addition, model predictions of spectral evolution and wave statistics in irregular depth-limited breaking waves are examined using the data sets of Mase and Kirby (1992) and Scott et al. (2004) (Section 3.3). Fig. 1 sketches the experimental layouts and the cross-shore locations of the available measurements for the cases considered here. Table 1 summarizes the associated input parameters.

Both spilling breaking (hereafter referred as TK1) and plunging breaking (hereafter referred as TK2) cases of Ting and Kirby (1994) are selected. This experiment has been widely used by other researchers to validate both non-hydrostatic models using surface- and terrain-following grid (Ma et al., 2014a; Bradford, 2011, 2012; Smit et al., 2013; Shirkavand and Badiei, 2014) and VOF-based numerical models (Ma et al., 2011; Lin and Liu, 1998a; 1998b; Bradford, 2000; Christensen, 2006; Lakehal and Liovic, 2011). A uniform grid of $\Delta x = \Delta y = 0.025$ m is used in the horizontal direction which is smaller than 1/150 of the wavelength in the transition regions. Grids with 4, 8, and 16 uniformly spaced σ -levels are used to examine the effects of varying vertical resolution. At the inflow boundary, the free surface location and velocities are calculated using the theoretical relations for cnoidal waves as given in Wiegel (1960).

We use both cases of Mase and Kirby (1992) (hereafter referred as MK1 and MK2). The two cases have different dispersive and nonlinear characteristics as summarized in Table 1. The data set of Mase and Kirby (1992) has been used in a number of previous studies of spectral wave modeling in the surf zone. In particular, MK2 has a high relative depth of $k_p h_0 \sim 2$ at the constant-depth region and a high relative steepness of $(k_p H_{rms})_0 \sim 0.16$, and thus is a highly dispersive and nonlinear case. In this experiment, irregular waves using the Pierson-Moskowitz spectrum were generated and allowed to propagate over a sloping planar bottom. The cross-shore location of the numerical wavemaker is set to be the first gage location (see Fig. 1b). The measured free surface and velocities determined from linear theory are used to prescribe the free

Table 1

Input parameters for the simulated depth-limited breaking cases. Here, h_0 is the still water depth in the constant-depth region in front of the wavemaker, $(kH)_0$ is the corresponding deep-water wave steepness of the generated wave, $\xi_0 = s/\sqrt{H_0/L_0}$ is the self similarity parameter, and s is the plane slope. For TK1 and TK2, H and T are the wave height and period of the cnoidal wave generated by the wavemaker. For S1 and S2, s is the averaged slope before the bar, assumed as $s \sim 1/12$. For the irregular wave cases, $T = T_p$ and $k = k_p$, where $()_p$ refers to the peak frequency of the incident waves. For S2, $H = H_{s0}$ is the deep-water characteristic wave height. For the rest of irregular wave cases, $H = H_{rms}$ at the first wave gauge.

Case no.	H (m)	T (s)	$(kH)_0$	$k_0 h_0$	ξ_0	breaking type	Exp.
TK1	0.125	2.0	0.126	0.6	0.20	regular, spilling	Ting and Kirby (1994)
TK2	0.128	5.0	0.015	0.2	0.59	regular, plunging	Ting and Kirby (1994)
S1	0.64	4.0	0.148	1.2	0.52	regular, plunging	Scott et al. (2004)
MK1	0.04	1.7	0.058	0.9	0.52	irregular, plunging	Mase and Kirby (1992)
MK2	0.04	1.0	0.161	2.0	0.31	irregular, spilling	Mase and Kirby (1992)
S2	0.59	4.0	0.136	1.2	0.54	irregular, plunging	Scott et al. (2004)

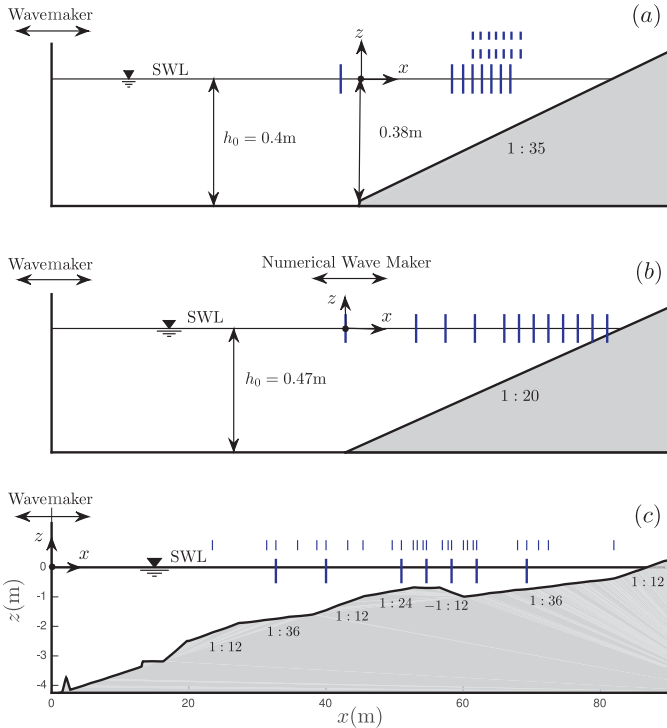


Fig. 1. Experimental layout of the simulated depth-limited breaking cases on a planar beach (a) Ting and Kirby (1994), (b) Mase and Kirby (1992) and a barred beach (c) Scott et al. (2004). Vertical solid and dashed lines in (a) show the cross-shore locations of the velocity and free surface measurements for TK1 and TK2 respectively. In (b), vertical solid lines show the cross-shore locations of the free surface measurements. In (c), vertical thick and thin solid lines show the cross-shore locations of the velocity and free surface measurements respectively.

surface and velocity boundary conditions at the inflow boundary by using the first 5000 Fourier components of the measured free surface time series, given by

$$\begin{aligned} \eta_{BC} &= \sum_{i=1}^n a_i \cos(\omega_i t + \epsilon_i) \\ u_{BC} &= \sum_{i=1}^n \frac{g a_i k_i}{\omega_i} \frac{\cosh(\sigma k_i D_{BC})}{\cosh(k_i D_{BC})} \cos(\omega_i t + \epsilon_i) - S D_i \\ w_{BC} &= \sum_{i=1}^n \frac{g a_i k_i}{\omega_i} \frac{\sinh(\sigma k_i D_{BC})}{\cosh(k_i D_{BC})} \sin(\omega_i t + \epsilon_i), \end{aligned} \quad (9)$$

where a_i and ϵ_i are the amplitude and phase of the i th Fourier component based on the measured free surface time series, k_i and ω_i are the wave number and angular frequency of the i th Fourier component based on the linear dispersion relation, n is the selected total number of Fourier components, $D_{BC} = h_{BC} + \eta_{BC}$, and SD_i is the linear Stokes drift associated with the i th Fourier com-

ponent. A uniform grid of $\Delta x = \Delta y = 0.015$ m and 0.01 m, which is approximately 1/150 of the dominant wavelength, is used in the horizontal direction for MK1 and MK2 cases, respectively. Resolutions of 4 and 8 σ -levels are used to examine the effects of varying vertical resolution.

We use the data set of Scott et al. (2004), including a regular breaking case (hereafter referred as S1) and irregular breaking case (hereafter referred as S2). The experiment was conducted in the large wave flume at Oregon State University, approximately 104 m long, 3.7 m wide, and 4.6 m deep. The bathymetry was designed to approximate the bar geometry for the averaged profile observed on October 11, 1994, of the DUCK94 field experiment at a 1:3 scale. The irregular waves of S2 were generated based on a TMA spectrum with a width parameter $\gamma = 20$ to generate the initial condition at the wavemaker. The cross-shore location of the numerical wavemaker is set to be as the initial position of the physical wavemaker. The measured free surface and velocities determined from linear theory are constructed at the wavemaker using the first 10 and 2000 Fourier components of the measured free surface time series (as given in Eq. (9)) in front of the wavemaker for S1 and S2 respectively. For both cases, a uniform grid of $\Delta x = \Delta y = 0.15$ m is used in the horizontal direction. Vertical resolutions of 4 and 8 σ -levels are used. The regular case S1 is also used by Jacobsen et al. (2014) to validate their two-dimensional (2-D) VOF/RANS model.

For regular wave cases, $\langle \rangle$ and $\overline{\langle \rangle}$ refer to phase and time averaging over five subsequent waves after the results reach quasi-steady state, respectively. We found that averaging over more than five waves results in approximately similar statistics in the shoaling and inner surf zone regions. Close to the initial break point, the phase-averaged wave crest elevation and the wave height slightly (less than 10%) decrease as the number of waves used for phase averaging increases. The corresponding measured averaged variables were calculated by averaging over 102 successive waves starting at a minimum of 20 min after the initial wavemaker movement for TK1 and TK2, and by phase averaging over 150 successive waves and ensemble averaging over at least 8 realizations for S1. For irregular wave cases, $\langle \rangle$ refers to long-time averaging over several minutes, or more than 250 waves. The mean water depth is defined as $\bar{D} = h + \bar{\eta}$, where h is the still water depth and $\bar{\eta}$ is the wave set-down/set-up. The numerical domain is extended beyond the maximum run-up, and the wetting/drying cells are treated as described in Ma et al. (2012, Section 3.4) by setting $D_{min} = 0.001$ m.

3.2. Wave height and free surface evolution in regular breaking waves

Fig. 2 shows the predicted and observed cross-shore distribution of wave heights $H = \langle \eta \rangle_{max} - \langle \eta \rangle_{min}$ in the shoaling, tran-

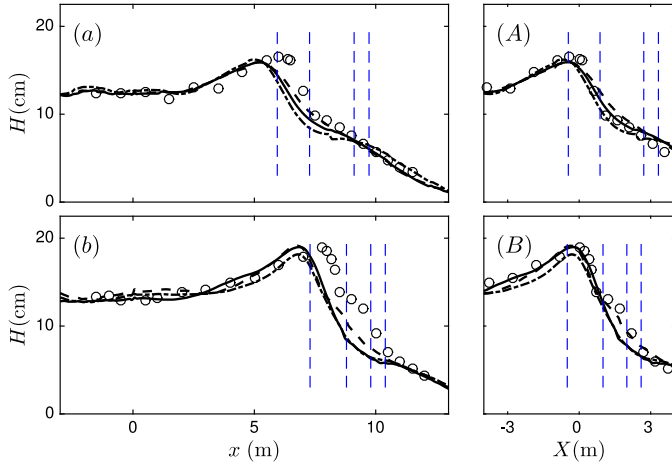


Fig. 2. Cross-shore distribution of the wave height $H = \langle \eta \rangle_{\max} - \langle \eta \rangle_{\min}$ for the regular depth-limited (a, A) spilling breaking case TK1 and (b, B) plunging breaking case TK2. In (A) and (B) the x location of the predicted and observed results are shifted with respect to the simulated and observed break point, where the former is 0.7 m far more offshore than the latter in both cases. Here, $X = x - x_b$ represents the horizontal distance from the break point. Comparison between NHWAVE results with 4 σ -levels (dashed lines), 8 σ -levels (solid lines), 16 σ -levels (dotted-dashed lines) and the measurements of Ting and Kirby (1994) (markers). Vertical dashed lines in (a, A) and (b, B) show the cross-shore locations of results shown in Figs. 3 and 4 respectively.

sition and inner surf zone regions for the regular spilling TK1 and plunging TK2 cases. Figs. 3 and 4 show the predicted and observed phase-averaged free surface elevations $\langle \eta \rangle$ at different cross-shore locations for TK1 and TK2, respectively. As in Ting and Kirby (1994), $x = 0$ is the cross-shore location at which $h = 0.38$ m. Here, $X = x - x_b$ is the horizontal distance from the initial break point, x_b . In Ting and Kirby (1994), the break point for spilling breakers was defined as the location where air bubbles begin to be entrained in the wave crest ($x_b = 6.40$ m), whereas for plunging breakers it was defined as the point where the front face of the wave becomes nearly vertical ($x_b = 7.8$ m). In the model, the break point is taken to be the cross-shore location at which the wave height starts to decrease. In the shoaling and inner surf zone regions, the model captures the evolution of the wave height and phase-averaged water surface elevations reasonably well using as few as 4 σ -levels. The predicted cross-shore location of the initial break point x_b , however, is slightly seaward of the observed location for both cases, regardless of the choice of vertical resolution (Fig. 2a,b); after shifting the results with respect to x_b , the predicted wave height decay rate (Fig. 2A,B) is consistent with observations. In addition, the wave crest elevation $\langle \eta \rangle_{\max}$ is underpredicted in the transition region compared with observations, as shown in the second row of Figs. 3 and 4. For TK2, Smit et al. (2013) reported the same trend as shown in their Figures 5 and 6.

Both the early initiation of breaking and underprediction of $\langle \eta \rangle_{\max}$ in the transition region have been reported in previous 2-D VOF/RANS simulations of depth-limited regular breaking waves on a planar beach; see, for example, Lin and Liu (1998a, Figure 3a), Lin and Liu (1998b, panel (a) of Figures 2 to 5), Bradford (2000, Figures 1 and 7) and Ma et al. (2011, Figure 9). Typical vertical grid spacing near the breaking crest in those studies were at least an order of magnitude smaller than in the present simulations using 4 σ -levels. Thus, this discrepancy may be due to the limitation of the $k - \epsilon$ turbulence closure model in a rapidly distorted shear flow such as breaking (Lin and Liu, 1998a), and cannot be due to a selected numerical resolution or the single-valued free surface assumption imposed in the σ -coordinate system. The effect of tur-

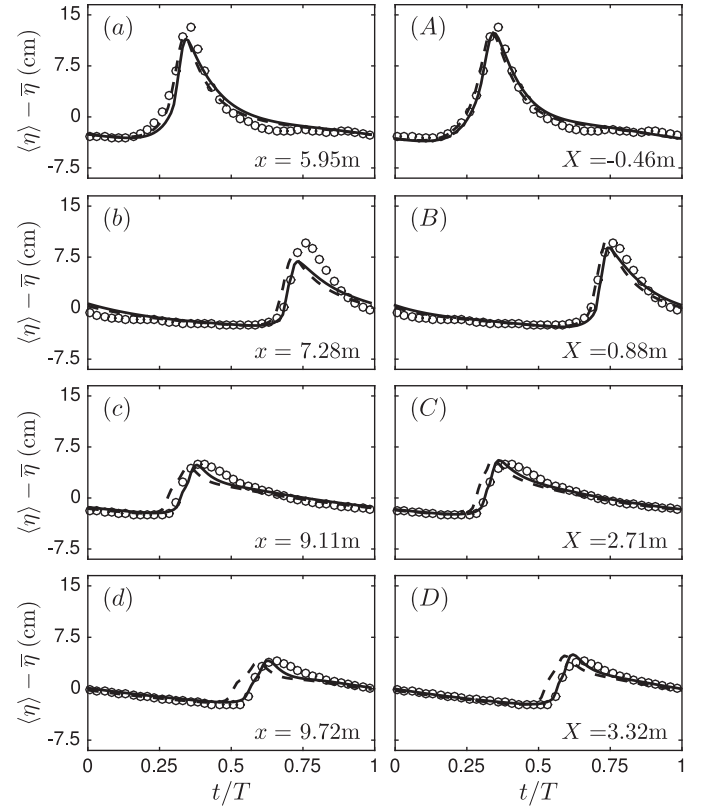


Fig. 3. Phase-averaged free surface elevations for the regular depth-limited spilling breaking case TK1 at (a–d) different cross-shore locations, and (A–D) different cross-shore locations in which the x location of the predicted and observed results are shifted with respect to the simulated and observed break point, where the former is 0.7 m far more offshore than the latter. Here, $X = x - x_b$ represents the horizontal distance from the break point. Comparison between NHWAVE results with 4 σ -levels (dashed lines), 8 σ -levels (solid lines) and the measurement (circle markers). The observed and simulated break points are at $x_b = 6.4$ m and 5.7 m, respectively.

bulent eddy viscosity estimations in the predicted bulk breaking-induced wave energy dissipation and wave height evolution is examined further in Section 5.

Fig. 5 shows the predicted and observed cross-shore distribution of the wave height H and still water level h for the regular plunging case over a barred beach S1 in the primary shoaling region up to the top of the bar ($x < 52.8$ m), the top of the bar ($52.8 \text{ m} < x < 56.5$ m), the shoreward face of the bar ($56.5 \text{ m} < x < 60$ m), and the secondary shoaling region after the bar ($x > 60$ m). As in Scott et al. (2004), $x = 0$ is the cross-shore location of the initial wavemaker location. The regular waves were observed to plunge at $x_b = 53$ m. The underprediction of the wave height near the initial break point, regardless of the various vertical resolutions, is similar to that discussed above. Compared with measurements, wave height decay in the breaking region and shoreward face of the bar is captured reasonably well using as few as 4 σ -levels. In the secondary shoaling region after the bar ($x > 60$ m), the overshoot of the wave height is not captured, as also seen in the VOF/RANS simulation of Jacobsen et al. (2014, Figure 4A). Fig. 6 shows the evolution of the predicted and observed $\langle \eta \rangle$ at different cross-shore locations before and after the bar. Although the time evolution of $\langle \eta \rangle$ is comparable with the measurements at all cross-shore locations, the crest is underpredicted near the initial break point as shown in panel (c) and after the bar as shown in panels (f) and (g). The secondary peak in the measured $\langle \eta \rangle$ at $x = 69.3$ m is also visible in the predicted results, while its crest elevation is underpredicted by the model. This secondary peak is

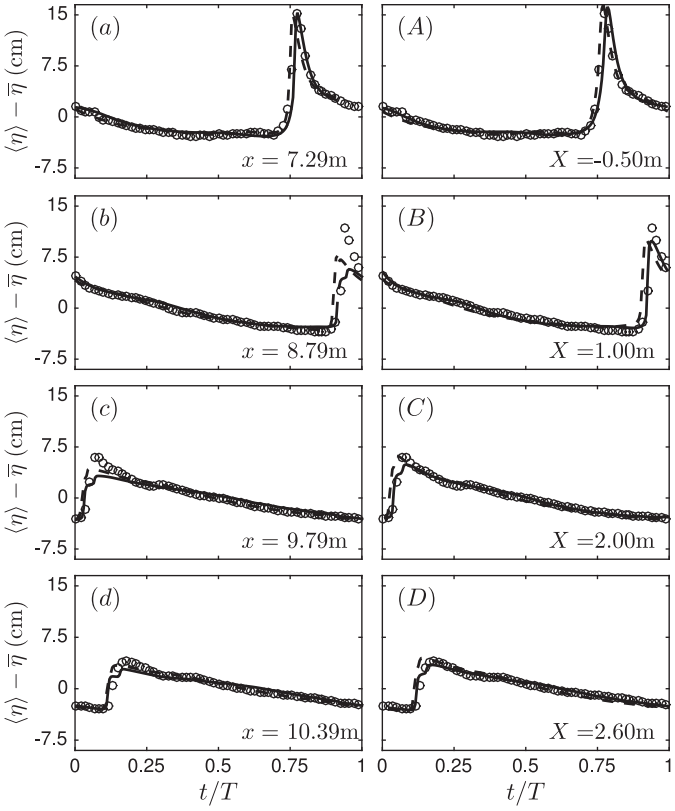


Fig. 4. Phase-averaged free surface elevations for the regular depth-limited plunging breaking case TK2 at (a–d) different cross-shore locations, and (A–D) different cross-shore locations in which the x location of the predicted and observed results are shifted with respect to the simulated and observed break point, where the former is 0.7 m far more offshore than the latter. Here, $X = x - x_b$ represents the horizontal distance from the break point.. Comparison between NHWAVE results with 4 σ -levels (dashed lines), 8 σ -levels (solid lines) and the measurement (circle markers). The observed and simulated break points are at $x_b = 7.8$ m and 7.1 m, respectively.

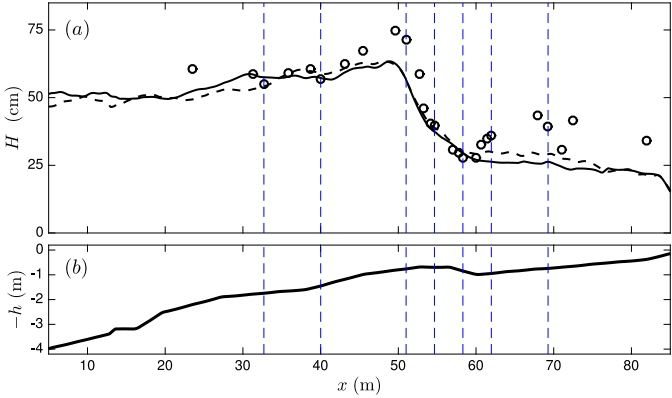


Fig. 5. Cross-shore distribution of (a) the wave height, $H = \langle \eta \rangle_{\max} - \langle \eta \rangle_{\min}$ and (b) the still water depth for the regular depth-limited plunging waves on a barred beach case S1. Comparison between NHWAVE results with 4 σ -levels (dashed lines), 8 σ -levels (solid lines) and the measurements of Scott et al. (2004) (circle markers). Vertical lines: the cross-shore locations of results shown in Fig. 6. The regular waves were observed to plunge at $x_b = 53$ m.

due to the generation of higher harmonics on top of the bar, which may then propagate with different phase speed than the primary wave.

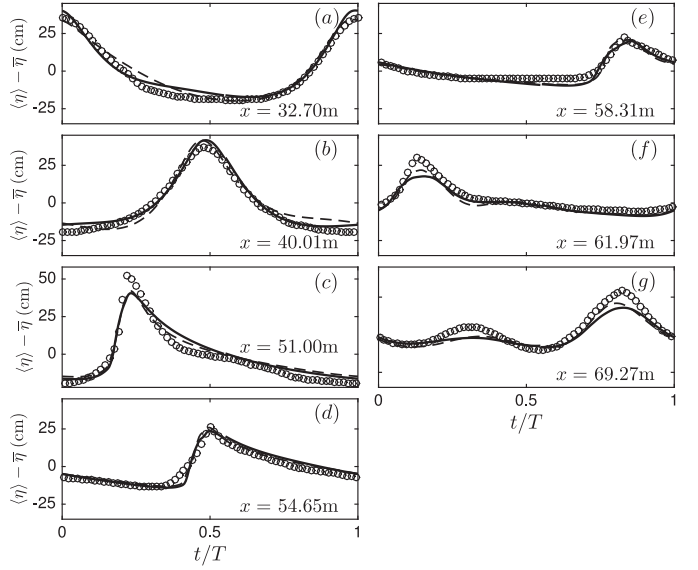


Fig. 6. Phase-averaged free surface elevations for the regular depth-limited breaking waves on a barred beach case S1 at different cross-shore locations, (a) $x = 32.7$ m, (b) $x = 40.0$ m, (c) $x = 51.0$ m, (d) $x = 54.65$ m, (e) $x = 58.31$ m, (f) $x = 61.97$ m, and (g) $x = 69.27$ m. Comparison between NHWAVE results with 4 σ -levels (dashed lines), 8 σ -levels (solid lines) and the corresponding measurements (circle markers). The regular waves were observed to plunge at $x_b = 53$ m.

Hereafter, we assess the model predictive skill using the statistical method developed by Willmott (1981) given by

$$\text{Skill} = 1 - \frac{\sum_{i=1}^N |\psi_{i,\text{sim}} - \psi_{i,\text{obs}}|^2}{\sum_{i=1}^N [|\psi_{i,\text{sim}} - \bar{\psi}_{\text{obs}}| + |\psi_{i,\text{obs}} - \bar{\psi}_{\text{obs}}|]^2}, \quad (10)$$

where ψ is the variable being compared, $\bar{\psi}$ is its sample mean value, and subscripts $(\cdot)_{\text{sim}}$ and $(\cdot)_{\text{obs}}$ stand for the simulated results and observations, respectively. This skill parameter measures the degree to which the observed deviations about the observed mean correspond with the predicted deviations about the observed mean. Perfect agreement between the simulated results and observations yields a skill of 1.0 whereas complete disagreement yields a skill of 0 (Willmott, 1981). The model predictive skills for $\langle \eta \rangle$ are above 0.94 for all cases, except for TK2 case using 4 σ -levels. In both TK1 and TK2, the increase of vertical resolution from 8 to 16 σ -levels has a negligibly small effect on the model skills for $\langle \eta \rangle$ in the surf zone.

3.3. Organized wave velocity evolution in regular breaking waves

Figs. 7 and 8 show the predicted and observed oscillatory part of the phase-averaged horizontal velocities $\langle u \rangle - \bar{u}$ normalized by the local phase speed \sqrt{gD} , in the shoaling, transition and inner surf zone regions close to the bed and trough level for TK1 and TK2, respectively. In the transition region of the spilling case TK1 (Fig. 7b,B), the shoreward velocity peak is underestimated by approximately 30% compared with observations, which is mainly due to the underprediction of η as shown in Fig. 3. The shoreward velocity peak near the trough level in the spilling case TK2 during the jet impact and splash-up is unresolved as shown in Fig. 8D. This is because of the velocity data resulting from the reproducible jet and splash-up structure is not represented in the simulated flow field. For the spilling case (Fig. 7) there is an apparent landward increasing phase lead in the results of the simulation with 4 σ -levels, indicating an overestimation of bore propagation speed at low vertical resolutions. This error is corrected at the higher resolutions of 8 and 16 σ -levels. The model predictive skills for

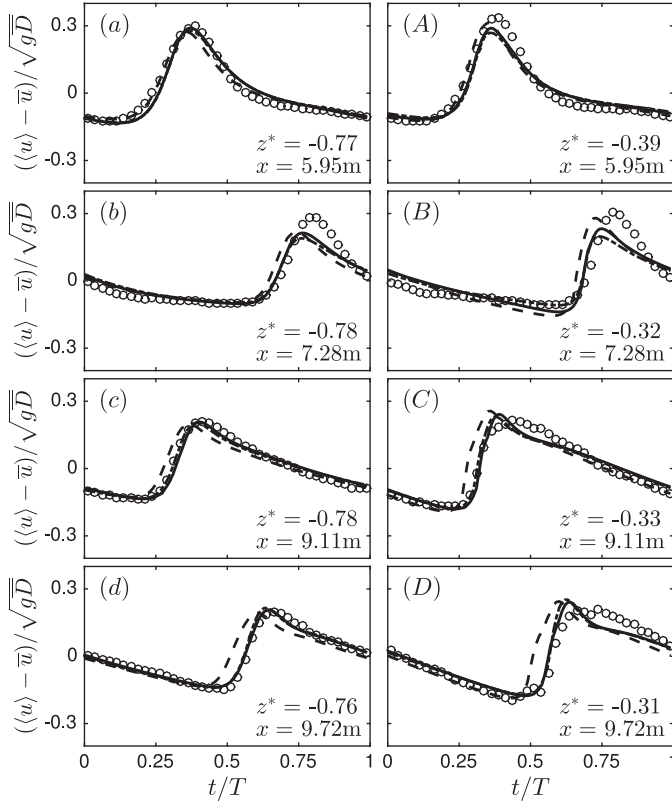


Fig. 7. Phase-averaged normalized horizontal velocities for the regular depth-limited spilling breaking case TK1 close to the (a–d) bed and (A–D) trough level, at different cross-shore locations before and after the initial break point. Comparison between NHWAVE results with 4 σ -levels (dashed lines), 8 σ -levels (solid lines), 16 σ -levels (dotted-dashed lines) and measurements (circle markers). Here, $z^* = (z - \bar{\eta})/\bar{D}$ where $\bar{D} = h + \bar{\eta}$ is the mean water depth. The observed and simulated initial break points are at $x_b = 6.4\text{ m}$ and 5.7 m respectively.

$\langle u \rangle - \bar{u}$ for both the spilling case TK1 and the plunging case TK2 are higher than 0.94 below the trough levels using as few as 4 σ -levels. In general, the model captures the evolution of $\langle u \rangle - \bar{u}$ below the trough level fairly reasonably both in time and space in both cases using as few as 4 σ -levels, and the increase of vertical resolution from 8 to 16 σ -levels has a small effect on the predicted $\langle u \rangle - \bar{u}$ below the trough level.

3.4. Power spectrum evolution and wave statistics in irregular breaking waves

The shape and energy content of wave spectra in nearshore regions are observed to have a considerable spatial variation over distances on the order of a few wavelengths due to continued wave-breaking-induced dissipation as well as triad nonlinear interactions between different spectral components (Elgar and Guza, 1985; Mase and Kirby, 1992). Here, we will examine the model prediction of the integral wave-breaking-induced energy dissipation as well as nonlinear wave-wave interaction compared with the corresponding measurements by looking at the evolution of the power spectral density, $S(f)$, from outside the surf zone up to the swash region.

Fig. 9 shows the variation of the computed $S(f)$ using 4 and 8 σ -levels for the irregular breaking cases MK1 and MK2 over a planar beach as well as the corresponding measured $S(f)$. The first 1000 data points were ignored both in the model result and the corresponding experiment for both cases. The measured signals then were split into 2048 data points segments. Each segment was multiplied by a cosine-taper window with the taper ratio of 0.05 to

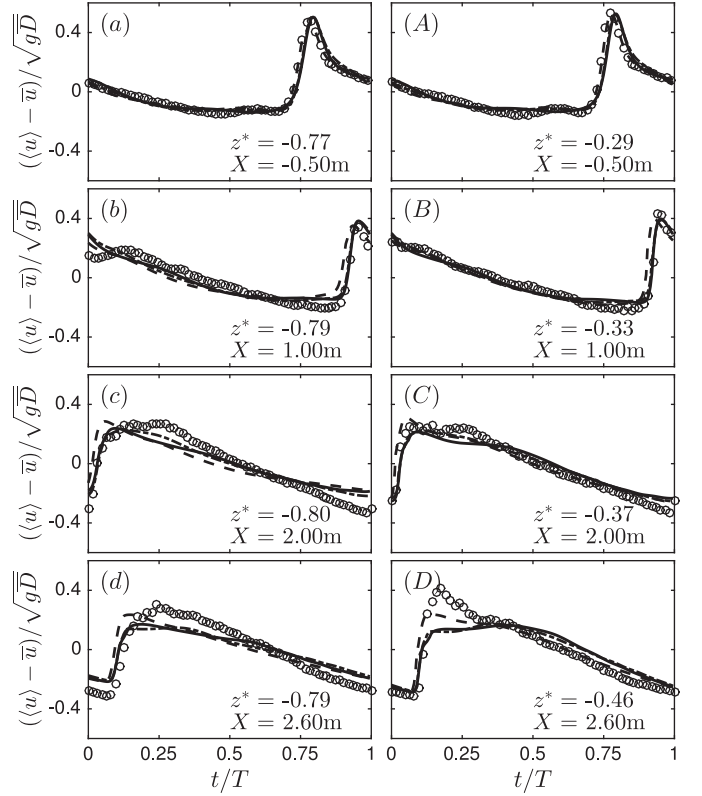


Fig. 8. Phase-averaged normalized horizontal velocities for the regular depth-limited plunging breaking case TK2 close to the (a–d) bed and (A–D) trough level, at different cross-shore locations before and after the initial break point at m. Comparison between NHWAVE results with 4 σ -levels (dashed lines), 8 σ -levels (solid lines), 16 σ -levels (dotted-dashed lines) and measurements (circle markers). Here, $z^* = (z - \bar{\eta})/\bar{D}$ where $\bar{D} = h + \bar{\eta}$ is the mean water depth and $X = x - x_b$ is the horizontal distance from the initial break point, where the observed and simulated initial break points are at $x_b = 7.8\text{ m}$ and 7.1 m respectively.

reduce end effects. The measured spectrum is obtained by ensemble averaging over the computed spectra of 8 and 7 segments for MK1 and MK2 respectively and then band averaging over 5 neighboring bands. The resulting averaged spectra of MK1 and MK2 have 80 and 70 degrees of freedom, respectively. The sampling rate was 25 Hz ($f_{Nyq} = 12.5\text{ Hz}$) for MK1 and 20 Hz ($f_{Nyq} = 10\text{ Hz}$) for MK2. The spectral resolution for MK1 and MK2 are $\Delta f = 0.06\text{ Hz}$ and 0.05 Hz , respectively. The spectrum for the computed wave field is obtained in a similar way, with the same spectral resolution and degrees of freedom. The first two rows of Fig. 9 show $S(f)$ outside the surf zone, while the other panels cover the entire surf zone up to a shallowest depth of $h \sim 3\text{ cm}$. We used the measured surface elevation time series at $h = h_0$ as an input, and thus infra-gravity waves appearing in the measured data are introduced in the domain as shoreward-propagating waves. The more pronounced predicted energy at this frequency range ($f/f_p < 0.5$, where f_p is the peak frequency) compared with measurements at shoreward cross-shore locations is mainly due to imposing the input low-frequency signal as a progressive wave at the numerical boundary while it was a standing wave in the measurement, and thus the input low-frequency climate is not exactly the same as in the measurement. Further, the absence of lateral side walls and the reflection from the upstream numerical boundary, which is located closer than the physical wavemaker used in the experiment to the plane slope, may explain some of the overpredicted energy in low-frequency wave components. Comparing with the measurements, the model captures the evolution of $S(f)$ and the integral wave-breaking-induced energy dissipation in the surf zone fairly well,

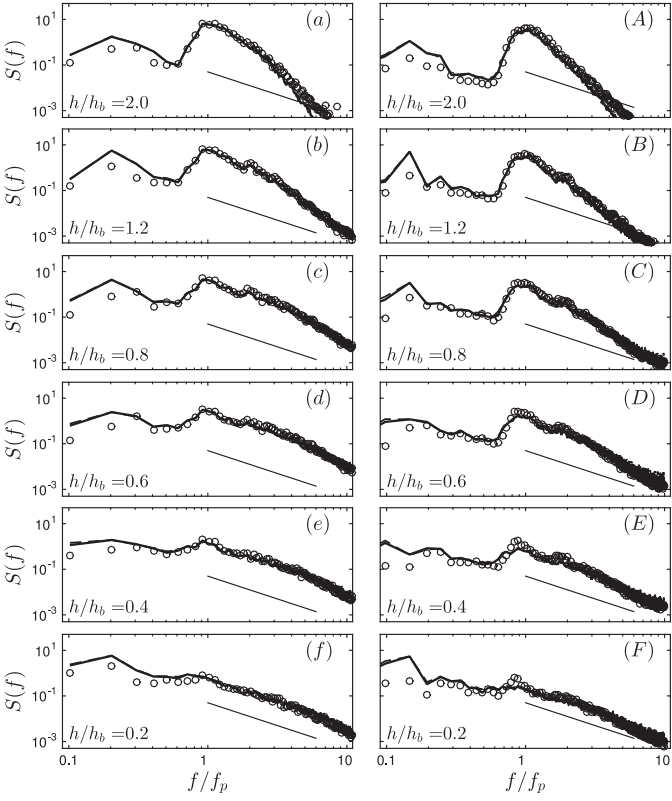


Fig. 9. Power spectral density evolution, $S(f)$ ($\text{cm}^2 \cdot \text{s}$), for the irregular depth-limited breaking cases (a–f) MK1 with $f_p = 0.6$ Hz and (A–F) MK2 with $f_p = 1.0$ Hz at different cross-shore locations. Comparison between NHWAVE results with 4 σ -levels (dashed lines), 8 σ -levels (thick solid lines) and the corresponding measurements (circle markers). Here, h is the still water depth, and h_b is the still water depth at $x = x_b$ ($h_b \sim 12.5$ cm). The solid lines show an f^{-2} frequency dependence.

using as few as 4 σ -levels. In addition, an asymptotic f^{-2} spectral shape of the wave spectrum in the inner surf zone (Kaihatu et al., 2007), due to the sawtooth-like shape of surf zone waves, is fairly reasonably captured by the model in both cases.

Second-order wave statistics, such as a significant wave height and a significant wave period, characterize the relative strength of irregular waves which needs to be estimated to determine wave forcing for different coastal or inner-shelf related calculations and designs. These may be defined based on the wave spectrum, $S(f)$, as a significant wave height $H_{m0} = 4m_0^{1/2}$ and the mean zero-crossing period $T_{m02} = (m_0/m_2)^{1/2}$, where $m_n = \int f^n S(f) df$, is the n th order moment of $S(f)$. To eliminate the infra-gravity and very high frequency wave effects, both the measured and computed ensemble-averaged $S(f)$ have been band-pass filtered with limits $0.25f_p < f < 8.0f_p$, and then H_{m0} and T_{m02} are obtained based on the resultant band-pass filtered spectra. The first and second rows of Fig. 10 show the cross-shore variations of the model predictions of H_{m0} and T_{m02} , using 4 and 8 σ -levels as well as the corresponding measured values for the irregular breaking cases over a planar beach MK1, MK2, and over a barred beach S2. Results show that NHWAVE correctly predict both the onset of breaking and the continued decrease of the wave height in the surf zone, indicating that the integral wave-breaking-induced energy dissipation is accurately captured. However, the wave height is slightly underpredicted in the transition region, as in the simulated regular breaking cases. The mean period T_{m02} is also accurately predicted. The model predictive skills for H_{m0} are 0.97, 0.9 and 0.98 for MK1, MK2 and S2 respectively. The predictive skills for T_{m02} are higher than 0.97 for all cases.

As waves propagate from deep into shallower depths, crests and troughs become sharper and wider, respectively. Furthermore, waves pitch forward, and in the surf zone, the waveform becomes similar to a sawtoothed form. Normalized wave skewness = $\eta^3 / (\eta^2)^{3/2}$, and asymmetry = $\bar{\mathcal{H}}(\eta)^3 / (\eta^2)^{3/2}$ (where \mathcal{H} denotes the Hilbert transform of the signal), are the statistical third-order moments characterizing these nonlinear features of a wave shape (Elgar and Guza, 1985; Mase and Kirby, 1992). Skewness and asymmetry are the statistical measures of asymmetry about horizontal and vertical planes, respectively. These third-order moments are potentially useful for sediment transport and morphology calculations (Hoefel and Elgar, 2003). Comparing with the measurements, the model fairly reasonably predicts the third-order wave statistics in the considered irregular waves, as shown in the third row of Fig. 10. Results show that the model captures nonlinear effects, including the energy transfer due to triad nonlinear interaction, in the entire water depths both in plunging and spilling dominated irregular breaking waves using as few as 4 σ -levels. Increasing the vertical resolution from 4 to 8 σ -levels has a negligibly small effect on the predicted wave statistics in all cases. The predictive skills for the normalized wave skewness are 0.87 and 0.86 for MK1 and MK2, respectively. The predictive skills for the asymmetry are 0.96 and 0.94 for MK1 and MK2, respectively. In S2, the model has approximately similar skills for the skewness and asymmetry before and on the top of the bar. However, the predicted transmitted waves after the bar are less skewed and more asymmetric about the vertical plane as opposed to observations. Note that Boussinesq wave models, both in the frequency domain and in the time domain, have also been shown to be capable to resolve power spectrum evolution in nearshore regions (see Kaihatu et al., 2007, and references therein).

4. Steepness-limited unsteady breaking focused wave packets

4.1. Model set-up and choice of experimental conditions

The data sets of Rapp and Melville (1990) and Tian et al. (2012) are considered to study the model capability and accuracy for wave-breaking-induced processes, including the evolution of the free surface, organized wave velocity (Section 4.2), total potential energy density, and power spectral density (Section 4.3), in steepness-limited unsteady breaking focused wave packets. Here, the model results for the two unsteady plunging breakers of Rapp and Melville (1990) (hereafter referred as RM1 and RM2) in an intermediate-depth regime with $k_c h \approx 1.9$ and one of the plunging cases of Tian et al. (2012) (hereafter referred as T1) in a deep-water regime with $k_c h \approx 6.9$ are presented, where k_c is the wave number of the center frequency wave of the input packet defined below. A uniform grid of $\Delta x = \Delta y = 0.023$ m and 0.005 m, which is approximately 1/100 of the dominant wavelength, is used in the horizontal direction for intermediate-depth cases (RM1 and RM2) and deep-water case (T1), respectively. Resolutions of 8, 16 and 32 σ -levels are used to examine the effects of varying vertical resolution.

In both experiments, breaking waves were generated using the dispersive focusing technique, in which an input packet propagates over a constant depth and breaks at a predefined time, t_b , and location, x_b . The input wave packet was composed of N sinusoidal components of steepness $a_i k_i$ where the a_i and k_i are the amplitude and wave number of the i th component. Based on linear superposition and by imposing that the maximum η occurs at x_b and t_b , the total surface displacement at the incident wave boundary can be obtained as (Rapp and Melville, 1990, Section 2.3)

$$\eta(0, t) = \sum_{i=1}^N a_i \cos[2\pi f_i(t - t_b) + k_i x_b], \quad (11)$$

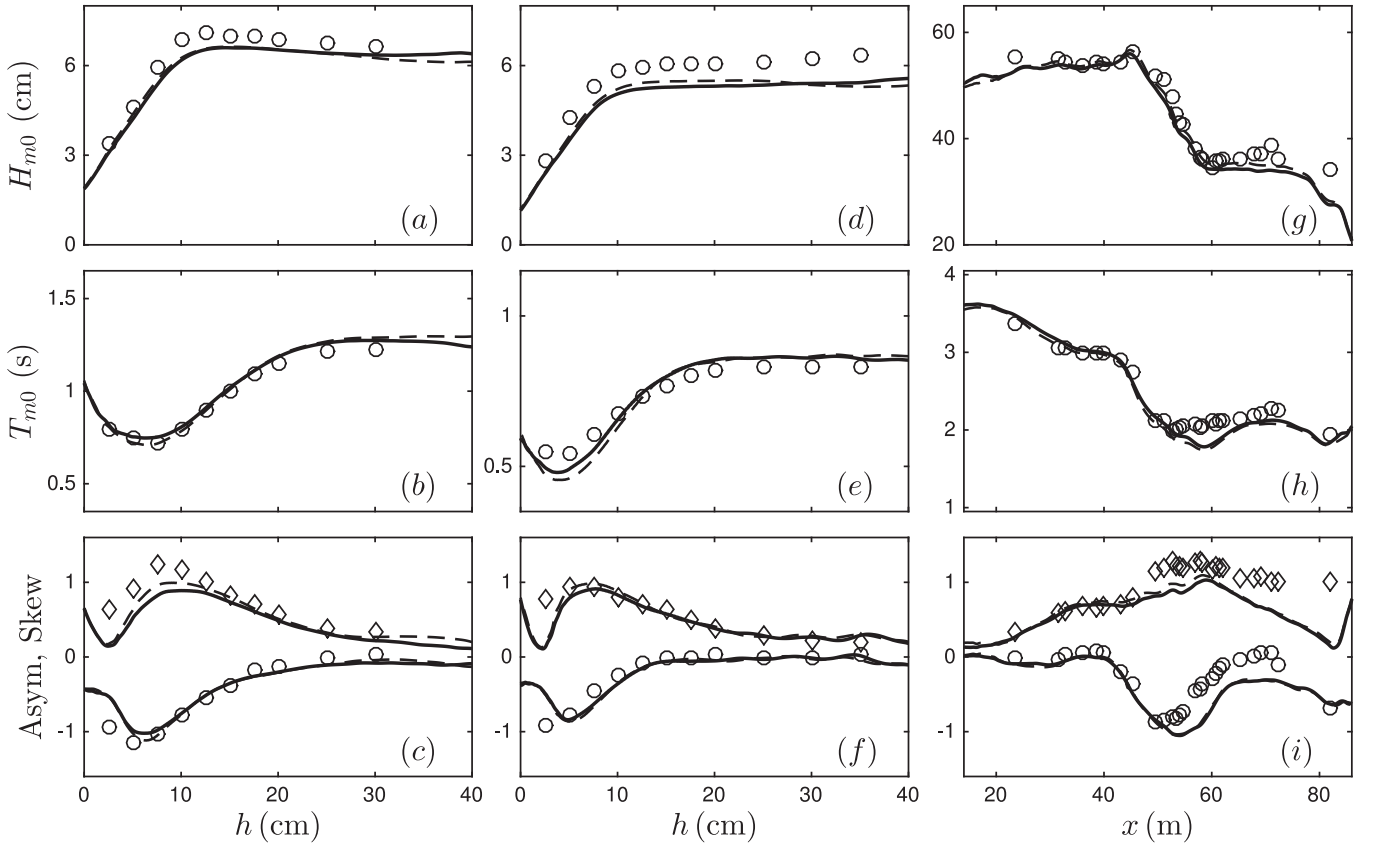


Fig. 10. Cross-shore variation of different second- and third-order wave statistics for the irregular depth-limited breaking cases (a, b, c) MK1, (d, e, f) MK2, and (g, h, i) S2. Comparison between NHWAVE results with 4σ -levels (dashed lines), 8σ -levels (solid lines) and the corresponding measurements (circle and diamond markers). Here, H_{m0} and T_{m0} are the characteristic wave height and period based on the power spectra of the signal, skewness $= \overline{\eta^3}/(\overline{\eta^2})^{3/2} > 0$ is the normalized wave skewness, asymmetry $= \overline{\mathcal{H}(\eta)^3}/(\overline{\eta^2})^{3/2} < 0$ is the normalized wave asymmetry, and h is the still water depth. In MK1 and MK2, the random waves were observed to break at $h_b \sim 12.5$ cm. In S2, the random waves were observed to be both plunging and spilling as far offshore as $x = 42$ m.

Table 2

Input parameters for the simulated focused wave packets. h is the still water depth, $S = \sum_{i=1}^N a_i k_i$ is the global steepness, N is the number of components in the packet, $a_i k_i$ is the component steepness, and the discrete frequencies f_i were uniformly spaced over the band $\Delta f = f_N - f_1$ with a central frequency defined by $f_c = \frac{1}{2}(f_N + f_1)$.

Case no.	h (m)	S	f_c (1/s)	$\Delta f/f_c$	N	breaking type
RM1	0.60	0.352	0.88	0.73	32	plunging
RM2	0.60	0.388	0.88	0.73	32	plunging
T1	0.62	0.576	1.70	0.824	128	plunging

where f_i is the frequency of the i th component. The discrete frequencies f_i were uniformly spaced over the band $\Delta f = f_N - f_1$ with a central frequency defined by $f_c = \frac{1}{2}(f_N + f_1)$. Different global steepnesses $S = \sum_{i=1}^N a_i k_i$ and normalized band-widths $\Delta f/f_c$ lead to spilling or plunging breaking, where increasing S and/or decreasing $\Delta f/f_c$ increases the breaking intensity (See Drazen et al. (2008) for more details). In the numerical wavemaker, free surface and velocities of each component are calculated using linear theory and then superimposed at $x = 0$. Sponge levels are used at the right boundary to minimize reflected waves. The input wave parameters for different cases are summarized in Table 2. The normalized time and locations are defined as

$$x^* = \frac{x - x_{ob}}{L_c}, \quad z^* = \frac{z}{L_c}, \quad t^* = \frac{t - t_{ob}}{T_c}, \quad (12)$$

where T_c and L_c are the period and wavelength of the center frequency wave of the input packet, respectively. Here, t_{ob} and x_{ob} are the time and location at which the forward jet hits the free surface, obtained from the corresponding VOF simulations.

4.2. Instantaneous free surface and organized wave velocity evolution

Fig. 11 shows the free surface evolution in the breaking region for RM1 using 8σ -levels. Fig. 12 shows the free surface time series at locations before and after the break point, showing that the model captures the free surface evolution up to the break point fairly accurately. The overall wave height decay is also predicted reasonably well. However, the sudden drop of the crest during active breaking is not resolved. Fig. 13 shows the normalized free surface elevations at $x^* = 0.60$ as well as the organized horizontal and vertical velocity at $x^* = 0.60$, $z^* = -0.025$ for RM1 using 8 and 16σ -levels and the corresponding measured ensemble-averaged signals. After breaking, the overprediction of crest and trough elevations as well as organized velocities compared with the measurements demonstrates the underprediction of the wave-breaking-induced energy dissipation by the model. The model predictive skills for the u and w time series at $x^* = 0.60$, $z^* = -0.025$ using 8σ -levels are 0.8 and 0.76 , respectively. The increase of vertical resolution from 8 to 16σ -levels increases the associated model skills to 0.88 and 0.84 respectively.

Fig. 14 shows the predicted and observed free surface elevations at different x locations for T1 using 8σ -levels. Nearly all the input wave components are in the deep-water regime ($k_i h > \pi$), and thus the packet is highly dispersive. Multiple breaking was

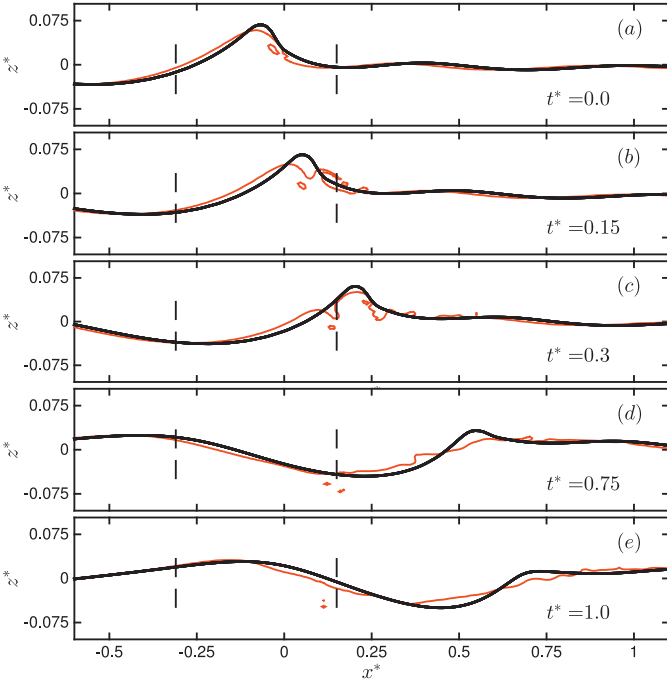


Fig. 11. Snapshots of the free surface evolution during active breaking for the steepness-limited intermediate-depth unsteady breaking case, RM1 at (a) $t^* = 0$, (b) $t^* = 0.15$, (c) $t^* = 0.3$, (d) $t^* = 0.75$, and (e) $t^* = 1$. Comparison between NHWAVE results with 8 σ -levels (thick black lines) and the VOF-based simulation of Derakhti and Kirby (2014b) (thin red lines). The free surface time series at the locations indicated by vertical dashed lines are shown in Fig. 12. Here, $x^* = (x - x_{0b})/L_c$, $z^* = z/L_c$, and $t^* = (t - t_{0b})/T_c$. (For interpretation of the references to color in this figure legend, the reader is referred to the web version of this article.)

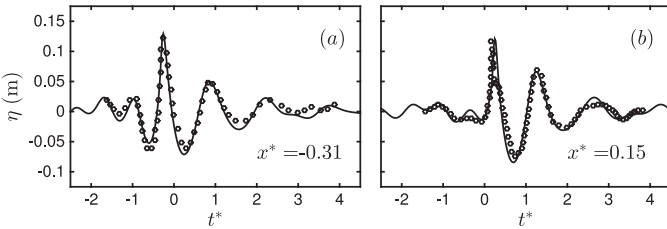


Fig. 12. Time series of the free surface evolution for the steepness-limited intermediate-depth unsteady breaking case, RM1 at (a) before and (b) after the break point ($x^* = 0$). Comparison between NHWAVE results with 8 σ -levels (solid lines) and the corresponding measurements of Rapp and Melville (1990) (circle markers).

observed in the experiment between $x^* \approx -1$ and $x^* \approx 1$, where $x^* = 0$ is defined based on the x location of the main breaking event in the packet. The model captures the packet propagation and evolution accurately. The model predictive skills for free surface time series at various cross-shore locations are between 0.96 and 0.98; approximately similar predictive skills were found by increasing the vertical resolution from 8 to 16 σ -levels. The focusing of dispersive waves before the break point can be seen at panels (a) through (c) with decrease in the number of waves and increase of the maximum crest elevation. Downstream of the breaking region (Fig. 14e, f), the results indicate that the wave height decay due to multiple unsteady breaking events, as well as dispersive properties of the packet, are captured by the model reasonably well.

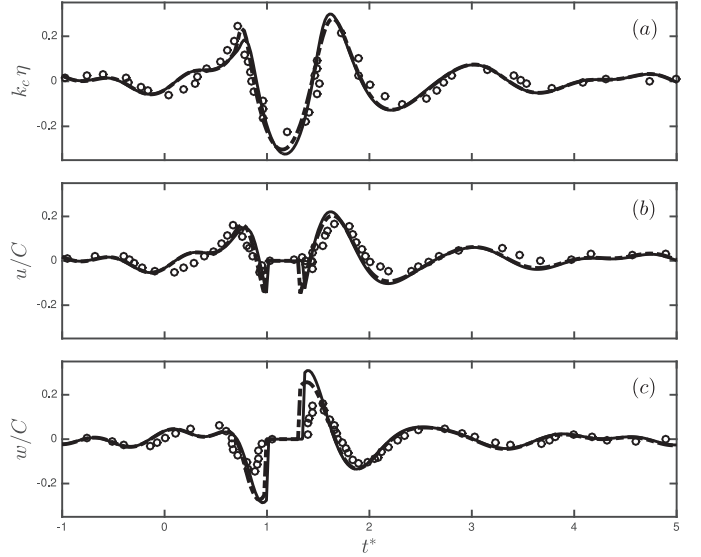


Fig. 13. Normalized ensemble-averaged (a) free surface elevations at $x^* = 0.6$, as well as (b) horizontal velocity and (c) vertical velocity at $x^* = 0.6$, $z^* = -0.025$ for RM1 using 8 σ -levels (solid lines) and 16 σ -levels (dotted-dashed lines). The circles are the measurements of the corresponding case adopted from Rapp and Melville (1990), Figures 40 and 41. Here, k_c and C are the wave number and the wave phase speed of the center frequency component in the incident packet.

4.3. Integral wave-breaking-induced energy dissipation and spectral evolution

In this section, the predicted integral wave-breaking-induced dissipation is compared with the corresponding measurements by looking at the evolution of the time-integrated energy density, $\rho g \bar{\eta}^2$, as well as the power spectral density. In this section, $(\bar{\cdot})$ refers to long-time integration over the entire wave packet. Strictly speaking, $\rho g \bar{\eta}^2$ is twice the time-integrated potential energy density, \bar{E}_p , and, to a good approximation, can be considered as the time-integrated total energy density far from the breaking region. By choosing an appropriate characteristic group velocity, $C_g \rho g \bar{\eta}^2$ is then used as an estimation of the time-integrated total horizontal energy flux. Thus, the spatial variation of $\rho g \bar{\eta}^2$ is related to total wave-breaking-induced energy dissipation for unsteady breaking waves, as explained by Derakhti and Kirby (2016) in detail.

Fig. 15(a) shows the variation of $\bar{\eta}^2/\bar{\eta}_1^2$ for the intermediate-depth case RM2 using 8 and 16 σ -levels and that predicted by the VOF-based simulation together with the experimental data, where subscript $(\cdot)_1$ refers to far upstream of the break point. The predicted integral dissipation is underestimated compared with the measurements. In addition, the predicted decay of \bar{E}_p occurs at a larger down wave distance compared with the measurements, and the sudden drop of the potential energy density is not resolved. Increasing the vertical resolution slightly improves the results in terms of the total wave energy dissipation and its rate. In these cases, the entire dissipation is imposed by the shock-capturing numerical scheme. In other words, the turbulence model has not been triggered, and modeled v_t is approximately zero. It is well known that the numerical dissipation applied by TVD numerical schemes decreases as the grid resolution in the horizontal direction increases. As shown in Fig. 15(b), by increasing the horizontal resolution from $\Delta x = 23$ mm to $\Delta x = 10$ mm, the total decay of \bar{E}_p becomes smaller, whereas the associated change in \bar{E}_p due to further decrease of Δx from 10 mm to 5 mm is negligibly small. A similar trend is observed in other cases (not shown).

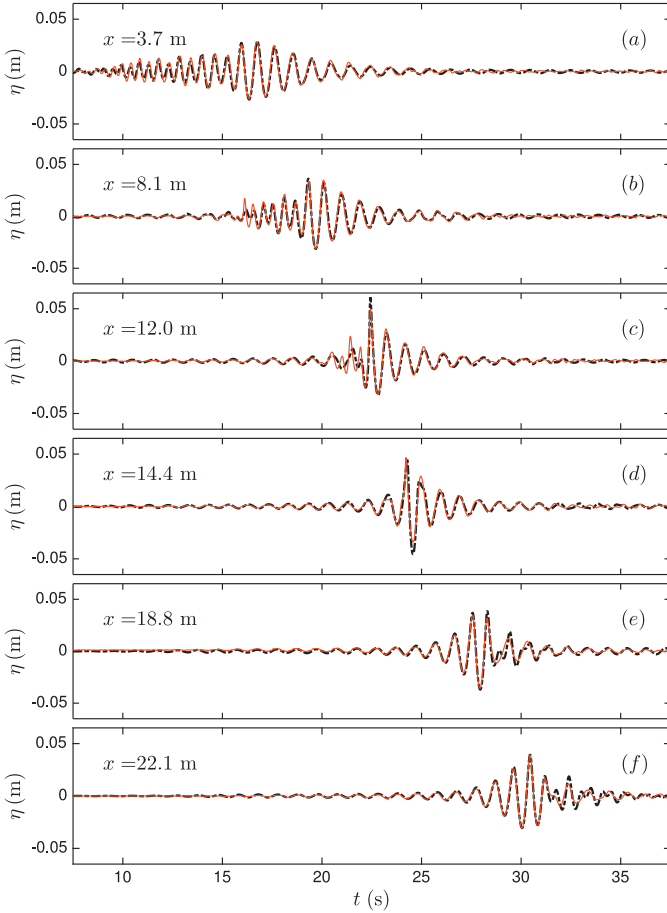


Fig. 14. Time series of the free surface evolution at different x locations, (a) $x = 3.7$ m, (b) $x = 8.1$, (c) $x = 12.0$, (d) $x = 14.4$, (e) $x = 18.8$, and (f) $x = 22.1$, for the steepness-limited deep-water unsteady breaking case, T1. Comparison between NHWAVE results with 8 σ -levels (black dotted dashed lines) and the measurement of Tian et al. (2012) (red solid lines). (For interpretation of the references to color in this figure legend, the reader is referred to the web version of this article.)

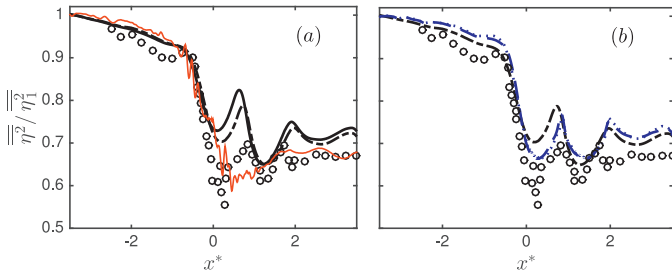


Fig. 15. Normalized time-integrated potential energy density, $\bar{E}_p = \bar{\eta}^2 / \bar{\eta}_1^2$, for the steepness-limited intermediate-depth unsteady breaking case RM2. Comparison between NHWAVE results with (a) $\Delta x = 23$ mm, 8 σ -levels (black thick solid line), $\Delta x = 23$ mm, 16 σ -levels (black dotted-dashed line), and the VOF-based simulation (red thin solid line); and (b) $\Delta x = 23$ mm, 16 σ -levels (black dotted-dashed line), $\Delta x = 10$ mm, 16 σ -levels (blue dashed line), $\Delta x = 5$ mm, 16 σ -levels (blue dotted line); and the corresponding measurements (circle markers). Here, subscript 1 refers to far upstream of the break point. (For interpretation of the references to color in this figure legend, the reader is referred to the web version of this article.)

Fig. 16 shows the evolution of different spectral components in the wave packet for the deep-water case T1 using 8 and 32 σ -levels, and the corresponding measurements of Tian et al. (2012). The measured spectrum is obtained by ensemble averaging over 5 runs and then band averaging over three neighboring bands (30 degrees of freedom) with a spectral resolution of $\Delta f = 0.075$ Hz, where the signal length is 40 s, and the sampling rate is 100 Hz.

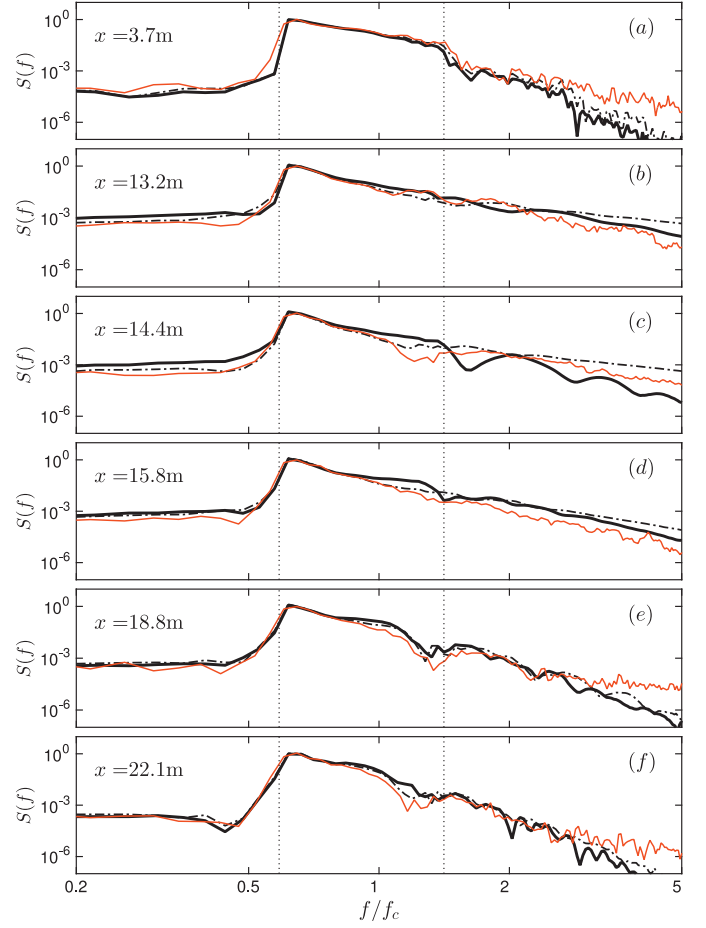


Fig. 16. Power spectral density evolution, $S(f)$ ($\text{cm}^2 \cdot \text{s}$) at different x locations, (a) $x = 3.7$ m, (b) $x = 8.1$, (c) $x = 12.0$, (d) $x = 14.4$, (e) $x = 18.8$, and (f) $x = 22.1$, for the steepness-limited deep-water unsteady breaking case, T1. Comparison between NHWAVE results with 8 σ -levels (black thick solid lines), 32 σ -levels (black dotted-dashed lines), as well as the measurements of Tian et al. (2012) (red thin solid lines). Vertical dotted lines indicate the frequency range of the input packet. (For interpretation of the references to color in this figure legend, the reader is referred to the web version of this article.)

The computed spectrum is based on a single realization with the same length and sampling rate. In general, the energy of the high frequency ($f/f_c > 2$) part of the spectrum is underestimated due to a relatively coarse vertical resolution of the model which cannot resolve fast decay of short-waves orbital velocities with depth. The nonlinear energy transfer into low-frequency components ($f/f_c < 0.5$), however, is fairly reasonably resolved. Energy is dissipated mostly in the frequency range $0.75 < f/f_c < 1.5$, as shown in panels (e) and (f). Close to the break point, the model does not capture the sudden dissipation of energy, especially for larger frequencies (Fig. 16c). The predicted spectrum becomes more similar to the measured spectrum as the packet propagates away from the breaking region.

5. Discussion

In the current single-phase study, the wave energy is dissipated through viscous and turbulent dissipation. The rate of modeled physical energy dissipation per unit volume is given by $\varepsilon = 2\rho(\nu + \nu_t)e_{ij}e_{ij}$, where ν_t and e_{ij} are the turbulent eddy viscosity and the rate of strain of the organized flow, respectively. During active breaking, both ν_t and the gradient of an ensemble-averaged velocity need to be reasonably estimated to accurately predict the total modeled physical wave-breaking-induced energy dissipation.

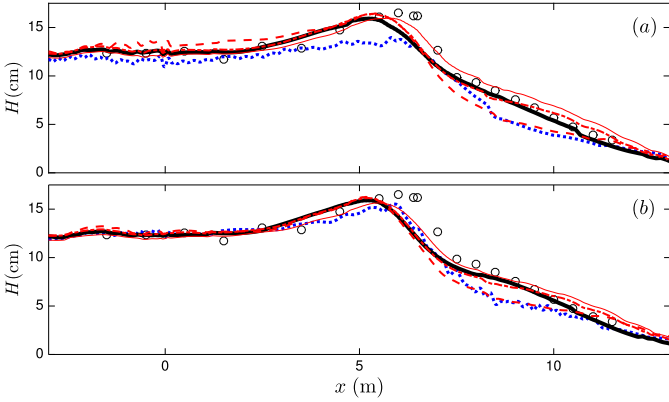


Fig. 17. Cross-shore distribution of the predicted wave height H using (a) 4 σ -levels, and (b) 8 σ -levels for the regular depth-limited spilling breaking case TK1. Comparison between the NHWAVE results in which v_t is calculated based on the $k - \epsilon$ turbulence model (black thick solid lines), $v_t = 0$ (blue dotted lines), $v_t/v = 100$ (red dashed lines), $v_t/v = 500$ (red dotted-dashed lines), and $v_t/v = 1000$ (red thin solid lines) as well as and the measurements of Ting and Kirby (1994) (markers). (For interpretation of the references to color in this figure legend, the reader is referred to the web version of this article.)

On the other hand, the energy may be dissipated by numerical dissipation (Bidadi and Rani, 2014) in regions with large horizontal gradients, such as a sharp wave-front, during active breaking. In this section, we examine the relative contribution of modeled physical wave energy dissipation and numerical dissipation to the total wave-breaking-induced energy loss in regular surface breaking waves.

Fig. 17 shows the cross-shore distribution of the predicted wave height H using 4 and 8 σ -levels for the regular depth-limited spilling breaking case TK1 together with the corresponding measurements. The different model predictions are obtained by using constant (0, 100 v , 500 v , and 1000 v , $v = 10^{-6}$ m 2 /s) and spatio-temporal varying v_t calculated based on the $k - \epsilon$ turbulence model. Results show that the underprediction of v_t , for example in the case with $v_t/v = 0$, results in the overprediction of the total wave-breaking-induced energy dissipation, and that the overprediction of v_t , for example in the case with $v_t/v = 1000$, results in the underprediction of total energy loss compared with observations. In other words, if the modeled physical dissipation has been underestimated, the considerable numerical dissipation imposed close to the wave front causes excessive wave energy loss and wave height decay. In the case of a significant overestimation of v_t , the velocity gradient decreases considerably, leading to an underestimation of the total wave energy loss and wave height decay. Further, in the absence of turbulent mixing ($v_t = 0$), unphysical high frequency waves are generated behind the sharp wave fronts in the surf zone, as shown in Fig. 18.

Bradford (2011, 2012) proposed several modifications to reduce the observed significant overprediction of wave heights in their surf zone breaking cases. Similar to NHWAVE, his model solves non-hydrostatic RANS equations in the σ -coordinate system, using an approximate Riemann solver for advection terms. Although the proposed modifications improved the predicted wave heights, the modified model still significantly overpredicted the wave heights in the inner surf zone, as shown in Bradford (2012, Figures 2, 4, 7, and 10). Results also showed that the increase of vertical resolution cannot improve the wave height predictions except in the outer surf zone (Bradford, 2012, Figure 10). Such overprediction of wave heights also was reported in the more recent study by Bradford (2014, Figures 9 and 14). Derakhti et al. (2016a) show that ignoring the surface slope terms in the surface dynamic boundary conditions, e.g., $\partial u / \partial \sigma = 0$ at the free surface, has a significant effect on the predicted wave shape and wave height evolution. For exam-

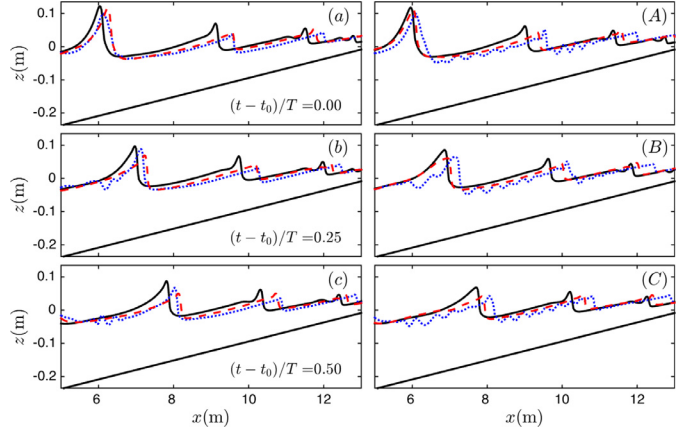


Fig. 18. Snapshots of the predicted free surface elevations, η , for the regular depth-limited spilling breaking case TK1 with (a, b, c) 4 σ -levels and (A, B, C) 8 σ -levels. Comparison between the NHWAVE results in which v_t is calculated based on the $k - \epsilon$ turbulence model (black solid lines), $v_t = 0$ (blue dotted lines), and $v_t/v = 100$ (red dashed lines). (For interpretation of the references to color in this figure legend, the reader is referred to the web version of this article.)

ple, their Figure 5 demonstrates that the wave height is considerably overpredicted in the surf zone by using the simplified boundary conditions. Based on above discussion, we believe that the observed overprediction of wave heights in the simulated surf zone breaking cases in Bradford (2011, 2012, 2014) is mainly because of using the simplified boundary conditions at the free surface which then provides an unphysical large values of v_t .

In addition, we note that the systematic delay in the initiation of breaking due to low vertical resolution reported in Smit et al. (2013, Figure 4) does not exist in our simulations, regardless of the relative magnitude of turbulent stresses. This suggests that the observed trend in Smit et al. (2013, Figure 4) is a result of the selected numerical scheme rather than a universal characteristic of the non-hydrostatic framework.

Finally, we should emphasize that although the underestimation of v_t results in a relatively greater numerical dissipation, it does not necessarily cause an overestimation of total wave-breaking-induced energy dissipation as it does in the surf zone. As shown in Section 4.3, in our steepness-limited breaking packets the total wave energy loss was underestimated compared with observations where the entire energy loss was due to numerical dissipation, and that the physical dissipation was approximately zero, $v_t \approx 0$.

6. Conclusions

In this paper, we examined wave-breaking predictions ranging from shallow- to deep-water conditions using a surface-and-terrain-following, shock-capturing 3-D non-hydrostatic model, NHWAVE (Ma et al., 2012), comparing results both with corresponding experiments and with the results of a VOF/Navier-Stokes solver (Ma et al., 2011; Derakhti and Kirby, 2014a,b). The new version of NHWAVE has been described in Derakhti et al. (2016a), including the new governing equations and consistent surface and bottom boundary conditions. We considered regular and irregular depth-limited breaking waves on planar and barred beaches as well as steepness-limited unsteady breaking focused wave packets in intermediate and deep depths. The same equations and numerical methods were used for the various depth regimes and involved no ad-hoc treatment, such as imposing hydrostatic conditions, in triggering breaking. Vertical grid resolution in all simulated cases was at least an order of magnitude coarser than that of typical VOF-based simulations. In Part 1 of this paper, we showed

that NHWAVE, as described in [Derakhti et al. \(2016a\)](#), accurately captured organized wave motions in terms of free-surface evolution, spectral evolution, organized wave velocity evolution and wave statistics using as few as 4 vertical σ -levels, without recourse to disabling of non-hydrostatic effects. In Part 2, we examine the model capability and accuracy in the reproduction of wave-breaking-induced turbulence and mean circulation. The main conclusions of the present study can be categorized as follows:

- (a) Depth-limited breaking waves: using as few as 4 σ -levels, the model was shown to predict cross-shore wave transformation in terms of the evolution of the wave height and phase-averaged water surface elevations, spectral evolution as well as the second- and third-order wave statistics both on planar and barred beaches as accurate as those predicted by typical VOF/RANS simulations. As it is explained by [Derakhti et al. \(2016a\)](#), the consistent boundary conditions significantly improved the predicted wave shapes and wave height evolution in depth-limited breaking waves compared with the commonly used simplified stress boundary conditions, ignoring the effects of surface and bottom slopes in the transformation of stress terms.
- (b) Steepness-limited breaking waves: it was shown that although the total wave-breaking-induced energy dissipation was underestimated, the model was capable of predicting the dispersive and nonlinear properties of different wave packet components before and after the break point, as well as the overall wave height decay and spectral evolution. This is one of the key advantages of the non-hydrostatic framework compared with the well-established Boussinesq models, which are only applicable in the shallow regions.
- (c) Modeled physical versus numerical dissipation during active breaking: it was illustrated that the underestimation of v_t resulted in a relatively greater numerical dissipation in the surf zone. However, it was found that the underestimation of v_t did not necessarily cause an overestimation of total wave-breaking-induced energy dissipation. For example, in the steepness-limited breaking packets the total wave energy loss was underestimated compared with observations in which the entire energy loss was due to numerical dissipation, and the physical dissipation was approximately zero, $v_t \approx 0$. The near-surface turbulence model for whitecap events, e.g., the model proposed by [Brocchini \(2002\)](#), is needed to provide an estimate of the surface stress associated with averaging over the turbulent patch on the free surface, with which the model will produce the turbulence field, leading to an enhanced eddy viscosity and an appropriate amount of wave-breaking-induced energy dissipation and wave height decay in the breaking region. Zero-stress surface boundary conditions also need to be improved in turbulent wave-front regions of surf zone breaking waves to accurately estimate turbulent eddy viscosity, with which the main part of the bulk wave-breaking-induced energy dissipation will capture by modeled physical dissipation given by $\varepsilon = 2\rho(v + v_t)e_{ij}e_{ij}$, where v_t and e_{ij} are the turbulent eddy viscosity and the rate of strain of the organized flow, respectively.

Acknowledgments

The authors gratefully thank Zhigang Tian, Marc Perlin, and Wooyoung Choi for providing the deep-water laboratory data. This work was supported by ONR, Littoral Geosciences and Optics Program (grant N00014-13-1-0124), NSF, Physical Oceanography Program (grant OCE-1435147) and Engineering for Natural Hazards (grants CMMI-1537100 and CMMI-1537232), and through the use of computational resources provided by Information Tech-

nologies at the University of Delaware. We thank the reviewers, whose thoughtful input led to significant improvements in the final manuscript.

References

- [Ai, C., Ding, W., Jin, S., 2014. A general boundary-fitted 3d non-hydrostatic model for nonlinear focusing wave groups. *Ocean Eng.* 89, 134–145.](#)
- [Banner, M.L., Peregrine, D.H., 1993. Wave breaking in deep water. *Ann. Rev. Fluid Mech.* 25, 373–397.](#)
- [Battjes, J.A., 1988. Surf-zone dynamics. *Ann. Rev. Fluid Mech.* 20, 257–291.](#)
- [Bidadi, S., Rani, S.L., 2014. Quantification of numerical diffusivity due to TVD schemes in the advection equation. *J. Comp. Phys.* 261, 65–82.](#)
- [Bradford, S.F., 2000. Numerical simulation of surf zone dynamics. *J. Waterway Port Coastal Ocean Eng.* 126, 1–13.](#)
- [Bradford, S.F., 2011. Nonhydrostatic model for surf zone simulation. *J. Waterway Port Coastal Ocean Eng.* 137, 163–174.](#)
- [Bradford, S.F., 2012. Improving the efficiency and accuracy of a nonhydrostatic surf zone model. *Coastal Eng.* 65, 1–10.](#)
- [Bradford, S.F., 2014. A mode split, Godunov-type model for nonhydrostatic, free surface flow. *Int. J. Numer. Methods Fluids* 75, 426–445.](#)
- [Brocchini, M., 2002. Free surface boundary conditions at a bubbly/weakly splashing air-water interface. *Phys. Fluids* 14, 1834–1840.](#)
- [Brocchini, M., Peregrine, D.H., 2001a. The dynamics of strong turbulence at free surfaces. Part 1. Description. *J. Fluid Mech.* 449, 225–254. doi:\[10.1017/S0022112001006012\]\(https://doi.org/10.1017/S0022112001006012\).](#)
- [Brocchini, M., Peregrine, D.H., 2001b. The dynamics of strong turbulence at free surfaces. Part 2. Free-surface boundary conditions. *J. Fluid Mech.* 449, 255–290.](#)
- [Christensen, E.D., 2006. Large eddy simulation of spilling and plunging breakers. *Coastal Eng.* 53, 463–485.](#)
- [Derakhti, M., Kirby, J.T., 2014a. Bubble entrainment and liquid-bubble interaction under unsteady breaking waves. *J. Fluid Mech.* 761, 464–506.](#)
- [Derakhti, M., Kirby, J.T., 2014b. Bubble Entrainment and Liquid-Bubble Interaction Under Unsteady Breaking Waves. Technical Report. CACR-14-06, Center for Applied Coastal Research, Dept. of Civil & Environmental Engineering, University of Delaware.](#)
- [Derakhti, M., Kirby, J.T., 2016. Breaking-onset, energy and momentum flux in focused wave packets. *J. Fluid Mech.* 790, 553–581.](#)
- [Derakhti, M., Kirby, J.T., Shi, F., Ma, G., 2015. NHWAVE: Model Revisions and Tests of Wave Breaking in Shallow and Deep Water. Technical Report. CACR-14-18, Center for Applied Coastal Research, Dept. of Civil & Environmental Engineering, University of Delaware.](#)
- [Derakhti, M., Kirby, J.T., Shi, F., Ma, G., 2016a. NHWAVE: consistent boundary conditions and turbulence modeling. *Ocean Modell.* doi:\[10.1016/j.ocemod.2016.09.002\]\(https://doi.org/10.1016/j.ocemod.2016.09.002\).](#)
- [Derakhti, M., Kirby, J.T., Shi, F., Ma, G., 2016b. Wave breaking from surf zone to deep-water in a non-hydrostatic RANS model. part 2: turbulence and mean circulation. *Ocean Modell.* doi:\[10.1016/j.ocemod.2016.09.011\]\(https://doi.org/10.1016/j.ocemod.2016.09.011\).](#)
- [Drazen, D.A., Melville, W.K., Lenain, L., 2008. Inertial scaling of dissipation in unsteady breaking waves. *J. Fluid Mech.* 611, 307–332.](#)
- [Elgar, S., Guza, R., 1985. Observations of bispectra of shoaling surface gravity waves. *J. Fluid Mech.* 161, 425–448.](#)
- [Hoefel, F., Elgar, S., 2003. Wave-induced sediment transport and sandbar migration. *Science* 299, 1885–1887.](#)
- [Jacobsen, N.G., Fredsoe, J., Jensen, J.H., 2014. Formation and development of a breaker bar under regular waves. part 1: model description and hydrodynamics. *Coastal Eng.* 88, 182–193.](#)
- [Kaihatu, J.M., Veeramony, J., Edwards, K.L., Kirby, J.T., 2007. Asymptotic behavior of frequency and wave number spectra of nearshore shoaling and breaking waves. *J. Geophys. Res.* 112, C06016. doi:\[10.1029/2006JC003817\]\(https://doi.org/10.1029/2006JC003817\).](#)
- [Lakehal, D., Liovic, P., 2011. Turbulence structure and interaction with steep breaking waves. *J. Fluid Mech.* 674, 522–577.](#)
- [Lin, P., Li, C.W., 2002. A \$\sigma\$ -coordinate three-dimensional numerical model for surface wave propagation. *Int. J. Numer. Methods Fluids* 38, 1045–1068.](#)
- [Lin, P., Liu, P.-F., 1998. A numerical study of breaking waves in the surf zone. *J. Fluid Mech.* 359, 239–264.](#)
- [Lin, P., Liu, P.-F., 1998. Turbulence transport, vorticity dynamics, and solute mixing under plunging breaking waves in surf zone. *J. Geophys. Res.* 103, 667–694.](#)
- [Lubin, P., Glockner, S., 2015. Numerical simulations of three-dimensional plunging breaking waves: generation and evolution of aerated vortex filaments. *J. Fluid Mech.* 767, 364–393.](#)
- [Ma, G., Chou, Y., Shi, F., 2014a. A wave-resolving model for nearshore suspended sediment transport. *Ocean Modell.* 77, 33–49.](#)
- [Ma, G., Kirby, J.T., Hsu, T., Shi, F., 2015. A two-layer granular landslide model for tsunami wave generation: theory and computation. *Ocean Modell.* 93, 40–55.](#)
- [Ma, G., Kirby, J.T., Shi, F., 2013a. Numerical simulation of tsunami waves generated by deformable submarine landslides. *Ocean Modell.* 69, 146–165.](#)
- [Ma, G., Kirby, J.T., Su, S., Figlus, J., Shi, F., 2013b. Numerical study of turbulence and wave damping induced by vegetation canopies. *Coastal Eng.* 80, 68–78.](#)
- [Ma, G., Shi, F., Hsiao, S., Wu, Y., 2014b. Non-hydrostatic modeling of wave interactions with porous structures. *Coastal Eng.* 91, 84–98.](#)
- [Ma, G., Shi, F., Kirby, J.T., 2011. A polydisperse two-fluid model for surf zone bubble simulation. *J. Geophys. Res.* 116, C05010. doi:\[10.1029/2010JC006667\]\(https://doi.org/10.1029/2010JC006667\).](#)
- [Ma, G., Shi, F., Kirby, J.T., 2012. Shock-capturing non-hydrostatic model for fully dispersive surface wave processes. *Ocean Modell.* 43, 22–35.](#)

- Mase, H., Kirby, J.T., 1992. Hybrid frequency-domain KdV equation for random wave transformation. In: Proceedings of the 23d International Conference on Coastal Engineering, pp. 474–487. Venice.
- Melville, W.K., 1996. The role of surface-wave breaking in air-sea interaction. *Ann. Rev. Fluid Mech.* 28, 279–321.
- Peregrine, D.H., 1983. Breaking waves on beaches. *Ann. Rev. Fluid Mech.* 15, 149–178.
- Perlin, M., Choi, W., Tian, Z., 2013. Breaking waves in deep and intermediate waters. *Ann. Rev. Fluid Mech.* 45, 115–145.
- Rapp, R.J., Melville, W.K., 1990. Laboratory measurements of deep-water breaking waves. *Philos. Trans. R. Soc. A*, 331, 735–800.
- Scott, C.P., Cox, D.T., Shin, S., Clayton, N., 2004. Estimates of surf zone turbulence in a large-scale laboratory flume. In: Proceedings of the 29th International Conference on Coastal Engineering, Portugal, pp. 379–391.
- Shi, J., Shi, F., Kirby, J.T., Ma, G., Wu, G., Tong, C., Zheng, J., 2015. Pressure decimation and interpolation (PDI) method for a baroclinic non-hydrostatic model. *Ocean Model.* 96, 265–279.
- Shirkavand, A., Badiei, P., 2014. The application of a Godunov-type shock capturing scheme for the simulation of waves from deep water up to the swash zone. *Coastal Eng.* 94, 1–9.
- Smit, P., Zijlema, M., Stelling, G., 2013. Depth-induced wave breaking in a non-hydrostatic, near-shore wave model. *Coastal Eng.* 76, 1–16.
- Tappin, D.R., Grilli, S.T., Harris, J.C., Geller, R.J., Masterlark, T., Kirby, J.T., Shi, F., Ma, G., Thingbaijam, K.K.S., Mai, P.M., 2014. Did a submarine landslide contribute to the 2011 Tohoku tsunami? *Mar. Geol.* 357, 344–361. doi:10.1016/j.margeo.2014.09.043.
- Tian, Z., Perlin, M., Choi, W., 2012. An eddy viscosity model for two-dimensional breaking waves and its validation with laboratory experiments. *Phys. Fluids* 24, 036601.
- Ting, F.C.K., Kirby, J.T., 1994. Observation of undertow and turbulence in a laboratory surf zone. *Coastal Eng.* 24, 51–80.
- Tonelli, M., Pettit, M., 2010. Finite volume scheme for the solution of 2d extended Boussinesq equations in the surf zone. *Ocean Eng.* 37, 567–582.
- Toro, E.F., 2009. *Riemann Solvers and Numerical Methods for Fluid Dynamics: A Practical Introduction*. Springer.
- Watanabe, Y., Saeki, H., Hosking, R.J., 2005. Three-dimensional vortex structures under breaking waves. *J. Fluid Mech.* 545, 291–328.
- Wiegel, R., 1960. A presentation of cnoidal wave theory for practical application. *J. Fluid Mech.* 7, 273–286.
- Willmott, C.J., 1981. On the validation of models. *Phys. Geogr.* 2, 184–194.
- Yakhot, V., Orszag, S., Thangam, S., Gatski, T., Speziale, C., 1992. Development of turbulence models for shear flows by a double expansion technique. *Phys. Fluids* 4, 1510–1520.
- Young, C., Wu, C.H., 2010. Nonhydrostatic modeling of nonlinear deep-water wave groups. *J. Eng. Mech.* 136, 155–167.
- Zhou, Z., Sangermano, J., Hsu, T.J., Ting, F.C.K., 2014. A numerical investigation of wave-breaking-induced turbulent coherent structure under a solitary wave. *J. Geophys. Res.* 119, 6952–6973.
- Zijlema, M., Stelling, G., Smit, P., 2011. SWASH: an operational public domain code for simulating wave fields and rapidly varied flows in coastal waters. *Coastal Eng.* 58, 992–1012.